Hydrothermal upgrading as an important tool for the REE mineralization in the Miaoya carbonatite-syenite complex, Central China

RONG-LIN MA[1,2], WEI TERRY CHEN[1,2,*], WEI ZHANG[1], AND YOU-WEI CHEN[1]

[1]State Key Laboratory of Ore Deposit Geochemistry, Institute of Geochemistry, Chinese Academy of Sciences, Guiyang 550081, China
[2]University of Chinese Academy of Sciences, Beijing 100049, China

ABSTRACT

Secondary hydrothermal reworking of REEs has been widely documented in carbonatites/alkaline rocks, but its potential role in the REE mineralization associated with these rocks is currently poorly understood. This study conducted a combined textural and in situ chemical investigation on the REE mineralization in the ~430 Ma Miaoya carbonatite-syenite complex, central China. Our study shows that the REE mineralization, dated at ~220 Ma, is characterized by a close association of REE minerals (monazite and/or bastnäsite) with pervasive carbonatization overprinting the carbonatites and syenites. In these carbonatites and syenites, both the apatite and calcite, which are the dominant magmatic REE-bearing minerals, exhibit complicated internal textures that are generally composed of BSE-bright and BSE-dark domains. Under BSE imaging, the former domains are homogeneous and free of pores or mineral inclusions, whereas the latter have a high porosity and inclusions of monazite and/or bastnäsite. In situ chemical analyses show that the BSE-dark domains of the apatite and calcite have light REE concentrations and $(La/Yb)_N$ values much lower than the BSE-bright areas. These features are similar to those observed in metasomatized apatite from mineral-fluid reaction experiments, thus indicating that the BSE-dark domains formed from primary precursors (i.e., represented by the BSE-bright domains) through a fluid-aided, dissolution-reprecipitation process during which the primary light REEs are hydrothermally remobilized. New, in situ Sr-Nd isotopic results of apatite and various REE minerals, in combination with mass balance calculations, strongly suggest that the remobilized REEs are responsible for the subsequent hydrothermal REE mineralization in the Miaoya complex. Investigations of fluid inclusions show that the fluids responsible for the REE mobilization and mineralization are CO_2-rich, with medium temperatures (227–340 °C) and low salinities (1.42–8.82 wt‰). Such a feature, in combination with C-O isotopic data, indicates that the causative fluids are likely co-genetic with fluids from coeval orogenic Au-Ag deposits (220–200 Ma) in the same tectonic unit. Our new findings provide strong evidence that the late hydrothermal upgrading of early cumulated REEs under certain conditions could also be an important tool for REE mineralization in carbonatites, particularly for those present in convergent belts where faults (facilitating fluid migration) and hydrothermal fluids are extensively developed.

Keywords: Apatite, calcite, REE mobilization and mineralization, hydrothermal upgrading, Miaoya carbonatite-syenite complex

INTRODUCTION

Carbonatites and/or associated alkaline rocks have been important providers of REEs, particularly the light REEs (Mariano 1989; Sheard et al. 2012), and thus are important exploration targets. Although there are more than 500 occurrences of carbonatites in the world and most of them contain elevated concentrations of REEs, only a few display economic potential to warrant exploitation (Woolley and Kjarsgaard 2008; Verplanck et al. 2016). Hence, unveiling key factors or processes leading to economic concentrations of REEs in these rocks has long been an attractive topic for ore genesis studies over the past decades (Xie et al. 2009; Pandur et al. 2014; Hou et al. 2015; Smith et al. 2016; Song et al. 2018). It was commonly accepted that processes responsible for REE enrichment in these rocks include primary magmatic concentration (e.g., the Mountain Pass deposit, California, U.S.A.) (Castor 2008), enrichment in late exsolved fluids through extreme fractionation of the carbonatitic or alkaline magmas, e.g., the Maoniuping deposit,

southwest (SW) China (Xie et al. 2009; Hou et al. 2015; Liu and Hou 2017), or a combination of the processes mentioned above (Pandur et al. 2014; Broom-Fendley et al. 2016). There is also increasing evidence showing that hydrothermal redistribution of REEs cumulated in early carbonatites or alkaline rocks, triggered by late autogenetic or external fluids, is also responsible for local REE enrichments, e.g., the Thor Lake and Strange Lake deposits, Canada (Salvi and Wiliams-Jones 1996; Sheard et al. 2012; Gysi and Williams-Jones 2013; Cheng et al. 2018; Cangelosi et al. 2020). However, the potential contributions of the hydrothermal reworking to REE mineralization in such kinds of deposits are still far from being clearly understood. Particularly, this unresolved issue likely gives rise to the controversies regarding ore genesis of some carbonatite-related REE deposits that show clear evidence of late hydrothermal overprints. A notable example could be the world's largest Bayan Obo REE-Nb-Fe deposit, where primary mineralogy and textures were overprinted by multiple hydrothermal events (Smith et al. 2015; and reference therein). In this deposit, late hydrothermal fluids (millions of years younger than

the carbonatites) were suggested to be the key for major REE mineralization (Ling et al. 2013; Yang et al. 2017), whereas others proposed that the early carbonatitic magmatism played a key role (Yang et al. 2019a).

The REE mineralization in the ~430 Ma Miaoya carbonatite-syenite complex, central China, is an ideal research target for evaluating the role of late hydrothermal metasomatism on REE mineralization in carbonatites and/or alkaline rocks. Although not mined currently, the potential REE reserve in the Miaoya complex was estimated to be 1.21 Mt. REE_2O_3 at 1.5 wt% (Qian and Li 1996). The REE mineralization was confirmed to be hydrothermal in origin and is spatially restricted to the complex, but direct U-Pb dating of REE minerals obtained much younger ages of 230–210 Ma (Xu et al. 2014; Ying et al. 2017; Zhang et al. 2019a). As such, few studies have suggested that the younger REE minerals could have formed from secondary remobilization of early REE mineralization (Ying et al. 2017, 2020; Zhang et al. 2019a, 2019b) or precipitated from external REE-rich fluids that overprinted the complex (Cimen et al. 2018). However, the reliability of these interpretations cannot be evaluated, as most of the data were obtained by analyses of bulk ore/rocks or mineral separates containing multiple generations of components (Ying et al. 2017, 2020; Cimen et al. 2018; Zhang et al. 2019a, 2019b). Moreover, the nature and sources of the causative fluids has not comprehensively been discussed.

In this study, we describe the styles of the REE mineralization in the Miaoya complex in detail, with emphasis on the textural relationships of REE minerals with other hydrothermal minerals and the internal features of various rock/ore-forming minerals, to re-establish the paragenetic sequence of the complex and associated mineralization/alteration. Moreover, utilizing electron microprobe (EMP) analysis, laser ablation-inductively coupled plasma-mass spectrometry (LA-ICP-MS), and laser ablation multi-collector inductively coupled mass spectrometer (LA-MC-ICP-MS) techniques, we have obtained in situ major-trace elemental and Sr-Nd isotopic compositions of various minerals forming during magmatic (e.g., apatite and calcite) and hydrothermal (e.g., monazite and bastnäsite) stages. The new data set, together with mass balance calculations based on compositions of altered apatite/calcite and unaltered counterparts, allows us to explore mobilization and mass transfer of REEs during fluid metasomatism, and thus, in turn, convincingly constrain the sources of REEs and the relative roles of early magmatic and late hydrothermal processes on the REE mineralization. In addition, Raman spectroscopic and microthermometric analyses were conducted to constrain the nature and potential sources of the fluids responsible for the REE mobilization and mineralization.

GEOLOGICAL BACKGROUND

The Qinling Orogenic Belt, extending east-west nearly 2500 km across Central China, is bounded by the North China Block to the north and the Yangtze Block to the south along the Sanbao and Longmenshan-Dabashan faults, respectively (Meng and Zhang 2000; Ratschbacher et al. 2003; Dong et al. 2011; Fig. 1a). The belt comprises four units separated by the Luanchuan, Shangdan, and Mianlue faults from the north southward, including the Southern North China Block, North Qinling unit, South Qinling unit, and Northern South China Block (Fig. 1b).

Formation of the orogenic belt involved the collision of North Qinling and South Qinling units during the Carboniferous and the final collision of the North China Craton and South China Craton during the Triassic (230–220 Ma) (Meng and Zhang 2000; Wu and Zheng 2013; Dong and Santosh 2016).

The South Qinling unit, where the Miaoya carbonatite-syenite complex is located, is comprised of a Precambrian basement covered by a 12 km thick sedimentary sequence Neoproterozoic to Triassic in age (Dong et al. 2011). The basement rocks are dominated by the Douling and Xiaomoling complexes in the north and the Wudang and Yaolinghe Groups in the south. The Neoproterozoic to Triassic cover sequences includes the strongly folded Sinian platform-type carbonate and clastic rocks, Cambrian-Ordovician limestones, Silurian shales, Devonian to Carboniferous clastic rocks with interlayered limestone, and Permian-Triassic sandstones (Mattauer et al. 1985; Ratschbacher et al. 2003; Dong et al. 2011; Wu and Zheng 2013; Liu et al. 2016). Silurian magmatism is widespread in this region, including ca. 430 Ma mafic-ultramafic dikes, volcanic rocks, and carbonatite-syenite complexes (e.g., Shaxiongdong and Miaoya) (Zhang et al. 2007; Xu et al. 2008). There are also a few early Mesozoic granitoids (250 to 190 Ma) randomly distributed in this belt (Xiao et al. 2017; Fig. 1b).

REE MINERALIZATION IN THE MIAOYA COMPLEX

The Miaoya complex is located in the southwestern margin of the Wudang Terrane in the South Qinling unit (Fig. 1b), covering an area of 6.5 km². It intruded the meta-quartz keratophyre of the Neoproterozoic Yaolinghe Group and the schist of the Late Silurian Meiziya Group along the Ankang-Desheng-Fangxian fault (Fig. 1c). The complex is composed mainly of syenites (90%) and carbonatites (7.5%), with xenoliths of country rocks (2.5%) mostly present in the margins (Figs. 1c and 2a–2c). The syenites are composed dominantly of K-feldspar (70 vol%) with subordinate but variable amounts of calcite (12 vol%), albite (10 vol%), apatite (1 vol%), zircon, Nb-bearing minerals (e.g., pyrochlore and columbite), and Fe-Ti oxides (e.g., ilmentite, magnetite, and rutile) (Fig. 2f). The carbonatites are generally present as stocks and/or dikes intruding the syenites (Figs. 1c and 2a) and can be classified as calciocarbonatites (>95%) and ferrocarbonatites (<5%) in terms of different mineral assemblages (Su et al. 2019). The calciocarbonatites are composed mainly of fine- to medium-grained calcite (0.1 to 2 mm) (85 vol%) and subordinate apatite (~9.5 vol%) with trace amounts of monazite, bastnäsite, parasite, allanite, K-feldspar, albite, quartz, biotite, zircon, Nb-bearing minerals (e.g., pyrochlore and columbite), and Fe-Ti oxides (e.g., ilmentite, magnetite, and rutile) (Fig. 2g). In contrast, the ferrocarbonatites are dominated by fine-grained ankerite (5–20 μm) (>70 vol%) with subordinate calcite (~10 vol%), bastnäsite (~5 vol%), and monazite (~2 vol%) and trace amounts of parisite, fluorite, and sulfides (Fig. 3f). Xu et al. (2014) has obtained zircon ages of 766 Ma for the syenites, but such ages were suggested to be unreliable by Zhu et al. (2016) and Ying et al. (2017), who both obtained a similar zircon age of 440 Ma for the syenites. Considering that an age of 766 Ma is comparable to those of the country rocks (i.e., volcanic rocks of the Yaolinghe Group), we speculated that the so-called "syenites" samples in Xu et al. (2014) could be xenoliths of the country rocks (particularly that the Miaoya complex contains 2.5 vol% xenoliths). For the carbonatites, Zhu et al. (2016) and
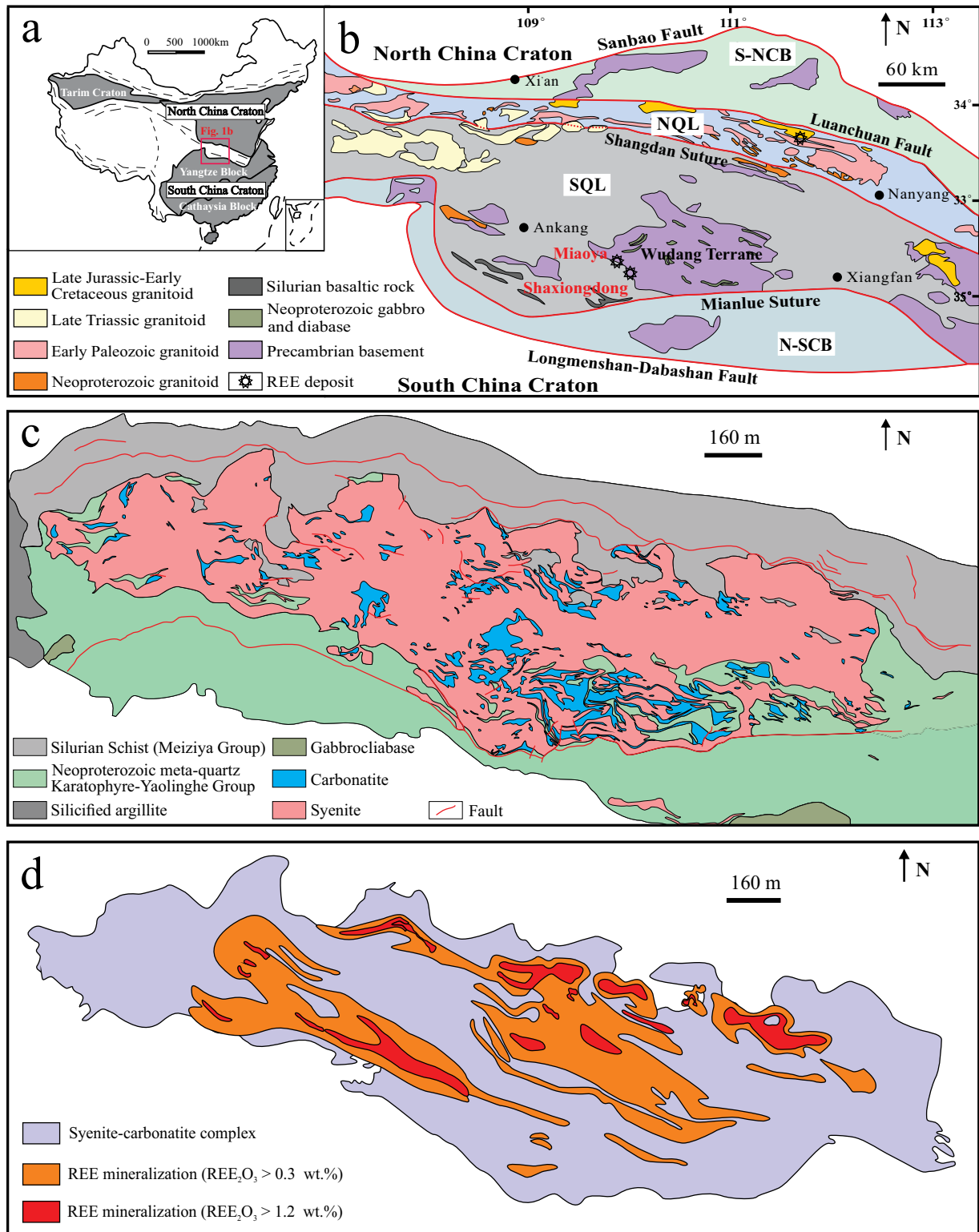
FIGURE 1. (**a**) Simplified tectonic map of China. (**b**) Geological sketch of the Qinling Orogenic Belt and the location of the Miaoya and Shaxiongdong deposits (modified from Zhang et al. 2019a). (**c**) Simplified geological map of the Miaoya complex (modified from Liu et al. 1984). (**d**) Simplified geological map showing the distributions of various REE ore bodies in the Miaoya complex (modified from Liu et al. 1984). Abbreviations: S-NCB = Southern North China Block; NQL = North Qinling; SQL = South Qinling; N-SCB = Northern South China Block. (Color online.)

Ying et al. (2017) obtained similar zircon ages of ~430 Ma. This age should be reliable as these zircon grains are characterized by low U and high Th/U ratios, similar to zircons crystallized from carbonatitic magmas (Yuan et al. 2008). These results indicate that both the carbonatites and syenites are broadly coeval and formed at around 440 to 430 Ma.

Both the carbonatites and syenites have undergone extensive carbonatization that is characterized by the presence of secondary, fine-grained calcite, ankerite, dolomite, quartz, and minor chlorite and Fe-oxides, which replace early carbonatite and syenite assemblages (e.g., calcite, K-feldspar, or apatite) (Figs. 2f, 2g, 3a, and 3b). The carbonatization is also associated with the formation of abundant carbonate-rich veinlets composed dominantly of calcite, dolomite, and/or quartz (Figs. 2d, 2e, 2h, and 2i).

The REE mineralization in the complex, dated at 230 to 210 Ma, is closely associated with the carbonatization, pervasively overprinting both the carbonatites and syenites as disseminated REE minerals or as REE mineral-rich veinlets or stockworks (Fig. 2e).

As such, the REE ores are essentially REE-mineralized syenites and carbonatites (Liu et al. 1984), such that there are no clear boundaries between the REE ores and hosting syenites or carbonatites (Figs. 2a and 2b). REE ore bodies were previously defined by these REE concentrations, and most of the defined ore bodies are lentoid and located mostly in the upper parts of the complex (Fig. 1d).

The REE minerals in the ores are dominated by monazite (20–300 μm), bastnäsite (1–35 μm), and/or allanite (1–60 μm) (Fig. 3). Parisite is also locally present, commonly replacing bastnäsite (Fig. 3h). The REE minerals are generally anhedral to subhedral and are closely intergrown with hydrothermal minerals, typically including fine- to medium-grained ankerite, calcite, sulfide, quartz, biotite, and phengite (Fig. 3). It is also noteworthy that some of the monazite grains commonly show an intimate association with relatively large apatite grains in both the syenites and carbonatites (Figs. 3a–3e). For example, they are mostly present as fine inclusions (1–20 μm) enclosed in or as irregular streaks distributed along fissures and margins of the apatite grains. These apatite
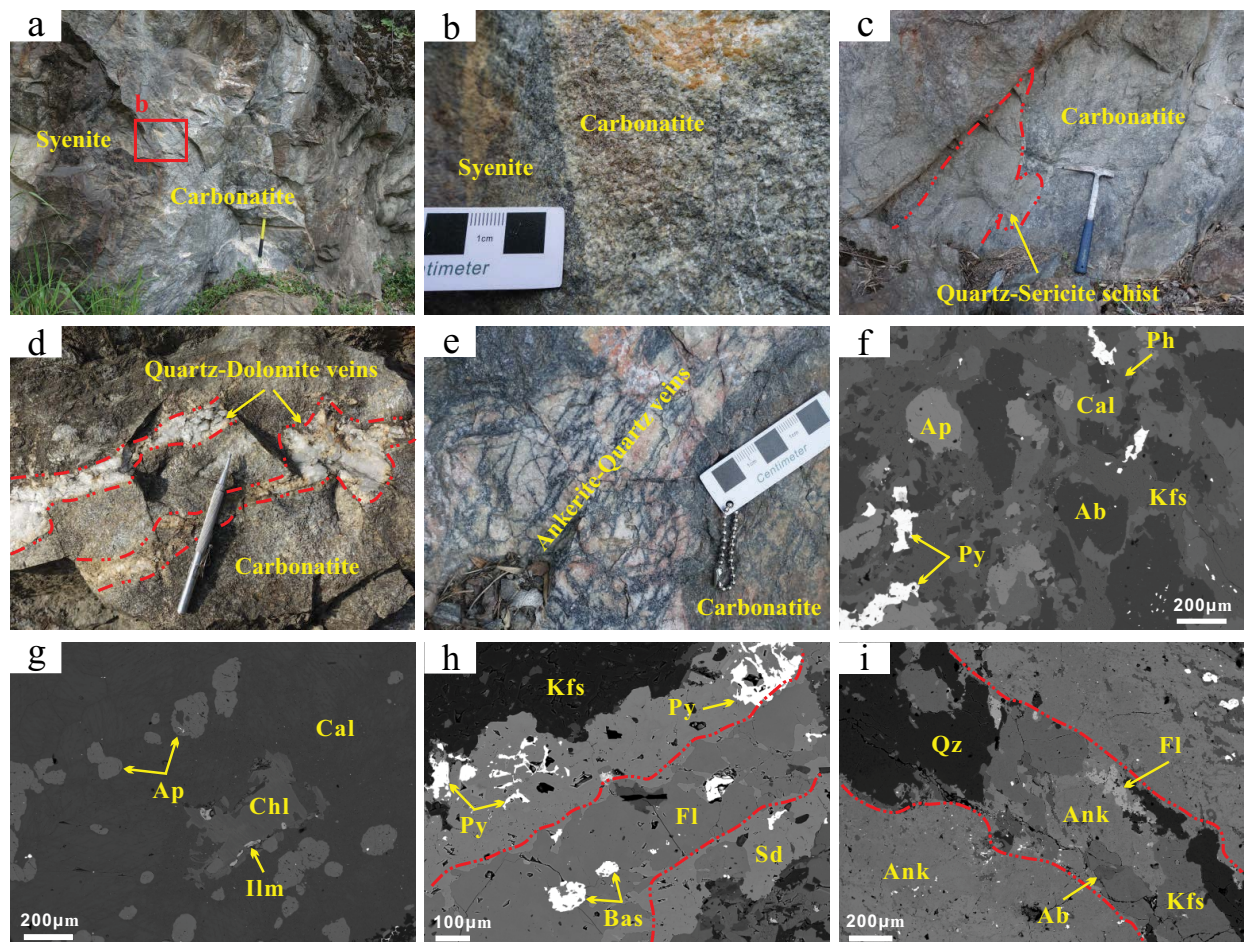

FIGURE 2. Field photos and BSE images of various rocks/ores in the Miaoya complex. (**a**) Carbonatites intruding syenites. (**b**) The boundaries between the carbonatites and syenites are sharp/straight. Note that the syenites have been carbonatized. (**c**) Xenoliths of wall rocks locally present in the carbonatites. (**d**) Veins of quartz + dolomite crosscutting carbonatites. (**e**) Veins of ankerite + quartz in the carbonatite crosscut by stockworks consisting of bastnäsite, pyrite, and graphite. (**f**) Fine-grained syenite composed dominantly of K-feldspar and albite with minor apatite. Note that the rock was extensively altered. (**g**) Carbonatite is composed of calcite and apatite with minor ilmenite and chlorite. (**h**) Veinlet of fluorite + bastnäsite crosscutting carbonatites. (**i**) Veinlet of K-feldspar + albite + quartz + ankerite crosscutting carbonatites. Abbreviations: Ab = albite; Ank = ankerite; Ap = apatite; Bas = bastnäsite; Cal = calcite; Chl = chlorite; Fl = fluorite; Ilm = ilmenite; Kfs = K-feldspar; Ph = phengite; Py = pyrite; Qz = quartz; Sd = siderite. (Color online.)
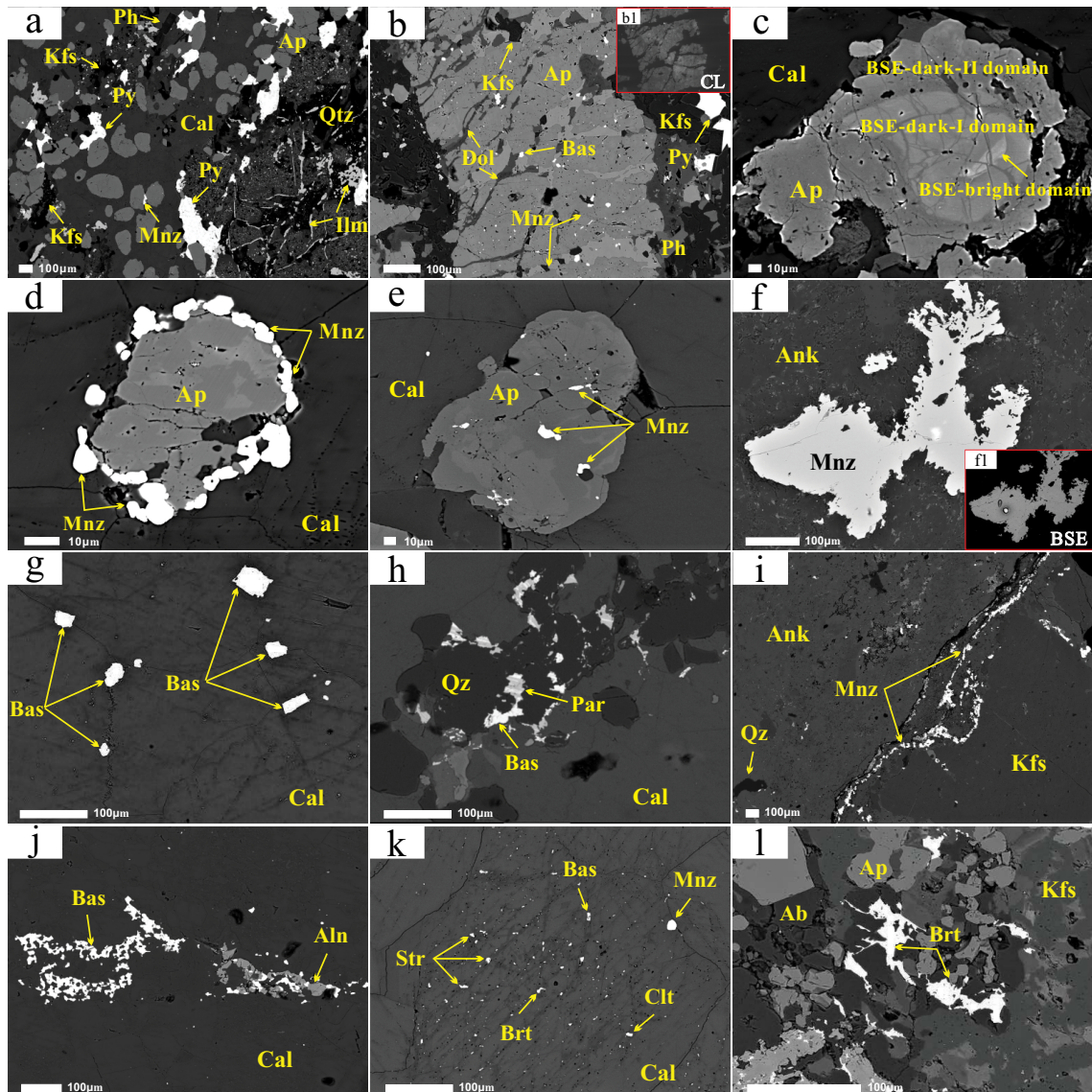
Figure 3. BSE images of diverse apatite grains in carbonatite and syenites and various REE ores. (**a**) Euhedral to subhedral apatite grains in carbonatites are intergrown with calcite and/or pyrite, eroded or replaced by phengite, K-feldspar, monazite, and quartz. (**b**) The apatite in carbonatites is extensively embayed by dolomite, phengite, biotite, pyrite, and K-feldspar. Note that the apatite contains abundant monazite and bastnäsite inclusions. b1 is a CL image of this grain. (**c**) Apatite in the carbonatite is extensively modified and contains three domains with irregular and sharp contacts. Note that BSE-dark-II domain occurs as strips that embay both the BSE-bright and BSE-dark-I domains. (**d**) Several monazite grains distributed along the margins of modified apatite in the carbonatites. (**e**) Relatively large monazite inclusions hosted in an extensively modified apatite grain in the carbonatites. (**f**) Disseminated monazites in ferrocarbonatite are irregular in shape, and homogenous under high-contrast BSE imagings (f1). (**g**) Disseminated bastnäsite in carbonatite. Note that the bastnäsite is mainly associated with the BSE-dark domains of the calcite. (**h**) Veinlet of bastnäsite + parisite + quartz in carbonatites. (**i**) Veinlet of monazite + ankerite + graphite in syenite. (**j**) Veinlets of batnäsite + allanite in carbonatite. (**k**) Abundant strontianite, barite, celestite, and bastnäsite grains mainly distributed in the BSE-dark areas in the calcite. (**l**) Veinlets of barite + albite + apatite in syenite. Abbreviations: Brt = barite; Clt = celestite; Dol = dolomite; Mnz = monazite; Par = parisite; Str = strontianite. Other abbreviations are the same as those in Figure 2. (Color online.)

grains, as will be illustrated below, exhibit complicated internal textures under backscattered electron (BSE) imagings.

On the basis of the macro- and micro-textural relationships of the mineral assemblages described above, we establish a paragenetic sequence for the formation of the Miaoya complex and subsequent REE mineralization, consisting of magmatic and hydrothermal stages (Online Material[1] Fig. OM1). The early

magmatic stage is characterized by the formation of magmatic minerals in early syenites and slightly later carbonatites. This includes dominantly K-feldspar and calcite, and subordinately apatite, albite, quartz, and biotite with trace amounts of REE minerals such as monazite and allanite (Figs. 2f and 2g) (Zhang et al. 2019a). The late hydrothermal stage is characterized by the formation of abundant REE minerals (monazite, bastnäsite,
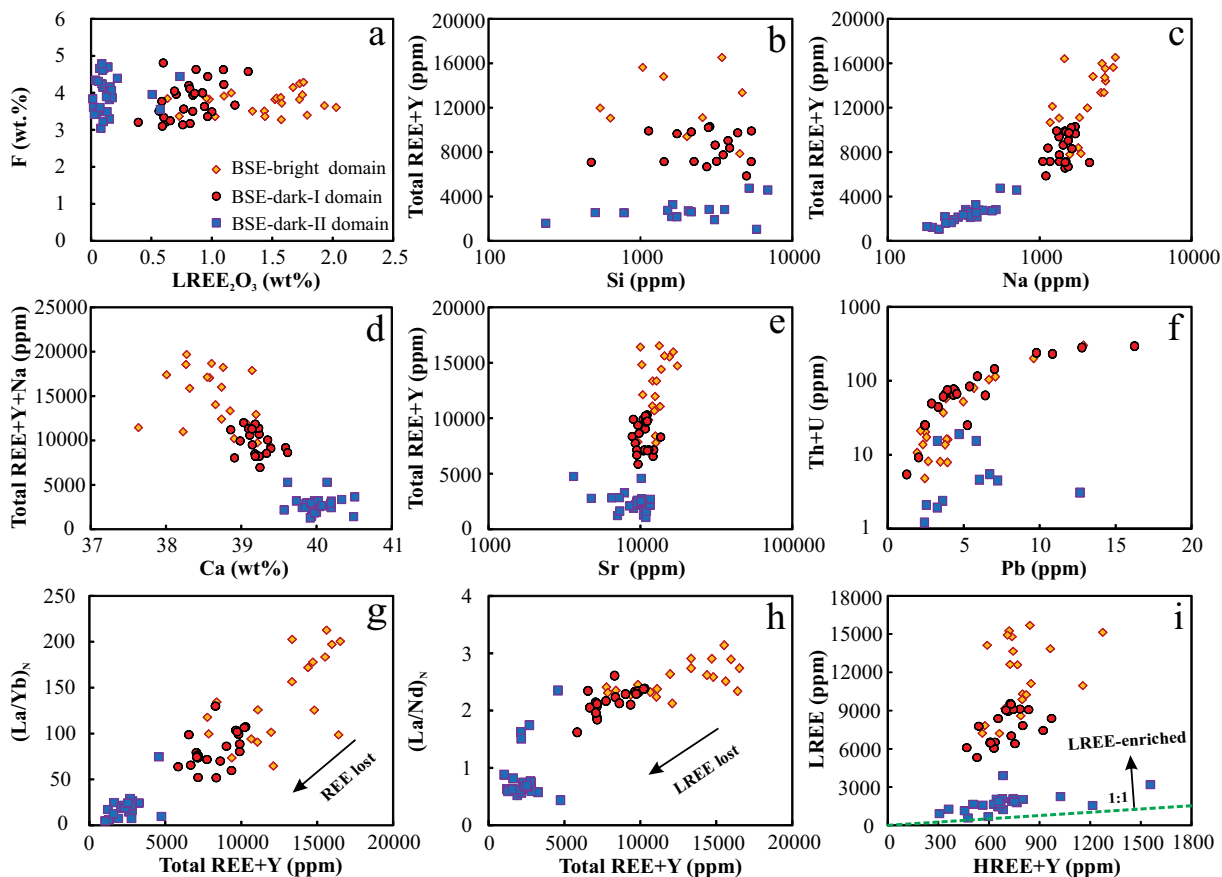
FIGURE 4. Bimodal plots of F vs. LREE$_2$O$_3$ (**a**), REE+Y vs. Si (**b**), REE+Y vs. Na (**c**), Ca vs. REE+Y+Na (**d**), REE+Y vs. Sr (**e**), Th+U vs. Pb (**f**), (La/Yb)$_N$ vs. REE+Y (**g**), (La/Nd)$_N$ vs. REE+Y (**h**), and LREE vs. HREE+Y (**i**) for different areas in the apatite. (Color online.)

allanite, and parisite) associated with pervasive carbonatization and variable amounts of calcite, K-feldspar, quartz, fluorite, dolomite, chlorite, and phengite (Fig. 3).

INTERNAL TEXTURES OF APATITE AND CALCITE

Detailed textural relationships between apatite and calcite were further investigated by scanning electron microscopy–cathode luminescence (SEM-CL). Detailed analytical methods are provided in Online Material[1] Methods.

Texture of apatite

Apatite grains in the carbonatites and syenites are broadly similar in terms of internal textures (Figs. 3a–3e). Under BSE imaging, these grains are generally composed of several domains with variable BSE intensities (Figs. 3b–3e). In most cases, these textures consist of only two parts consisting of BSE-bright and BSE-dark domains (Figs. 3d and 3e), but in rare cases they may consist of three parts named as BSE-bright, BSE-dark-I, and BSE-dark-II domains of which this last domain is darkest under BSE imaging (Fig. 3c). The contacts among different domains in each apatite grain are generally irregular and sharp (Figs. 3c–3e). The BSE-bright domains are commonly homogeneous without any cracks and are present mostly in the centers of the apatite grains (Fig. 3c). In contrast, the BSE-dark domains, including I and II, are mostly present along the margins

of the apatite grains and are irregular, and rich in pores, cracks, and mineral inclusions. Notably, the BSE-dark-II domains, if present, occur as irregular strips and patches embaying both the BSE-bright and BSE-dark-I domains (Fig. 3c).

The apatite grains are closely associated with fine-grained REE minerals dominated by monazite with minor bastnäsite (Fig. 3). These REE minerals are either present as fine inclusions enclosed in the BSE-dark domains or as anhedral grains distributed along the apatite grain rim (Figs. 3a–3e), where calcite and sulfide inclusions are also commonly present. In the latter case, the REE minerals are relatively large, subrounded to angular in shape, and are generally homogenous even under high-resolution BSE imagings (Fig. 3d).

Texture of calcite

Calcite is the predominant mineral of the calciocarbonatites in the Miaoya complex and is commonly present as subhedral to anhedral grains with grain sizes highly variable (0.1 to 2 mm) (Fig. 2g). Similar to the apatite, the calcite also shows complex internal textures that are composed of BSE-bright and BSE-dark domains under high-contrast BSE imaging (Fig. 3k). The BSE-bright domains are generally homogeneous and free of inclusions or voids, whereas the BSE-dark domains contain abundant voids and mineral inclusions dominated by fine-grained REE minerals, e.g., monazite, bastnäsite, and/or parisite, and minor pyrite, celestite, barite, and strontianite (Fig. 3k).

MINERAL CHEMISTRY

Major and trace elemental compositions of different minerals were obtained by EMP analytical and LA-ICP-MS (Figs. 4–7) techniques, respectively. Analytical methods and results are available in Online Material[1] Methods and Online Material[1] Table OM1–OM5, respectively.

Apatite chemistry

Apatite grains in the altered carbonatites and syenites, including both the BSE-bright and BSE-dark domains, are all fluorapatite characterized by high F (3.04–4.79 wt%) but low Cl or OH contents (<0.02 wt%) (Fig. 4a; Online Material[1] Table OM1). The BSE-bright domains have CaO (52.40–54.72 wt%) slightly lower than the BSE-dark-I and -II domains (53.42–56.52 wt%), whereas the P_2O_5 contents in different domains are broadly similar (Figs. 7a–7c). In terms of trace elements, LA-ICP-MS analyses show that the BSE-bright domains have mean Sr (12 647 ppm), Na (2095 ppm), Ga (86 ppm), Ge (40 ppm), Ba (18 ppm), and Zr (21 ppm) values remarkably higher than BSE-dark-I and II domains (Online Material[1] Table OM2). Such chemical differences among different domains are also clearly revealed by the EMP mapping (Fig. 7).

In terms of REE concentrations, LA-ICP-MS analyses indicate that all the domains are similarly enriched in LREEs relative to HREEs (Fig. 4i) but exhibit dramatically different REE contents and chondrite-normalized REE patterns (Figs. 4 and 5). The BSE-bright domains have the highest REEs (total: 7778–16 525 ppm), followed by the BSE-dark-I (5845–10 287 ppm) and BSE-dark-II domains (1048–4742 ppm) (Online Material[1] Table OM2). Notably, total contents of REE+Y in all the domains are positively correlated with Na and Sr but do not exhibit a clear correlation with Si (Figs. 4b, 4c, and 4e). Moreover, there is a negative correlation between REE+Y+Na and Ca (Fig. 4d). In the chondrite-normalized REE diagrams, both the BSE-bright and BSE-dark-I domains exhibit smoothly, right-dipping REE patterns (Figs. 5a and 5b), even though the BSE-bright domains tend to have relatively high LREE contents, $(La/Yb)_N$ and $(La/Nd)_N$ values (Figs. 4g and 4h). In contrast, the BSE-dark-II domains exhibit distinctly inverted "U"-like REE patterns in which the LREE portions are almost flat, corresponding to much lower values of $(La/Yb)_N$ (4.8–74.6) and $(La/Nd)_N$ (0.4–2.3) (Fig. 5c; Online Material[1] Table OM2). Instead, the HREE patterns are broadly parallel to those of the BSE-bright and BSE-dark-I domains (Fig. 5). All the domains have undistinguishable Eu anomalies with δEu values varying from 0.87 to 1.22.
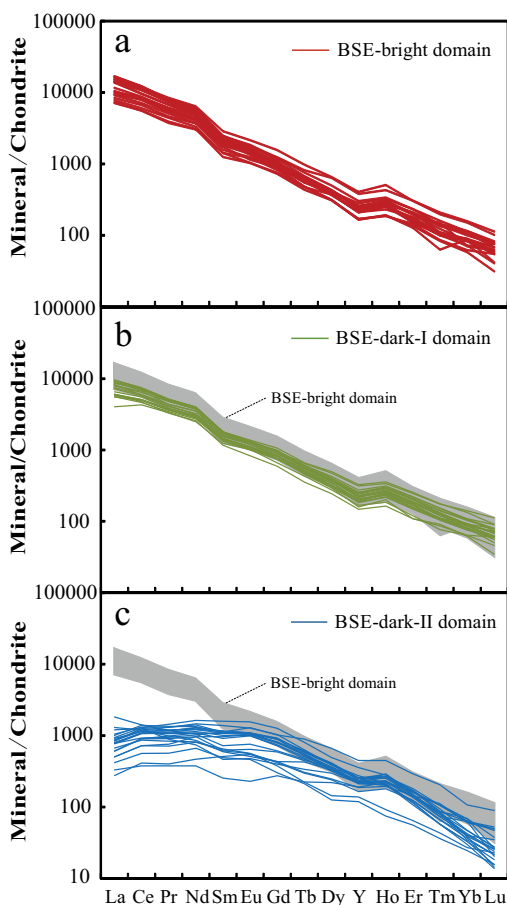

FIGURE 5. Chondrite-normalized REE patterns from the BSE-bright (**a**), BSE-dark-I (**b**), and BSE-dark-II (**c**) areas in the apatite. (Color online.)
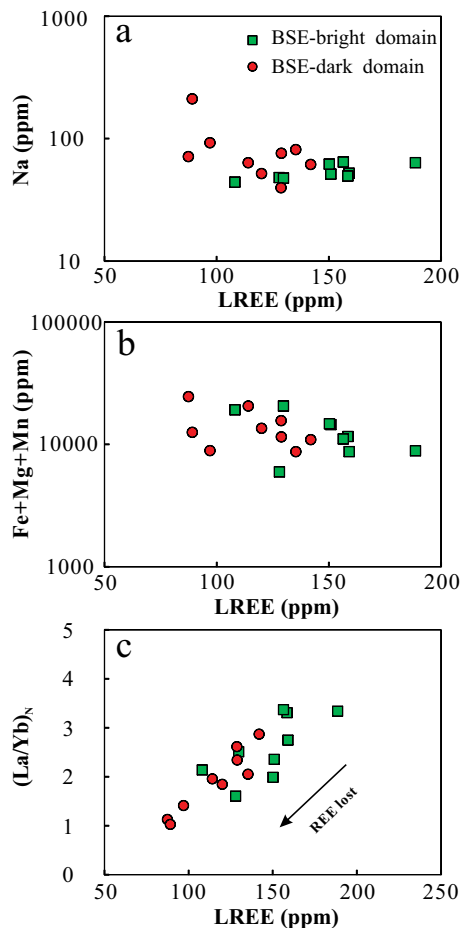

FIGURE 6. Bimodal plots of Na vs. LREE (**a**), Fe+Mn+Mg vs. LREE (**b**), and $(La/Yb)_N$ vs. LREE (**c**) from different areas in the calcite. (Color online.)

Calcite chemistry

Both the BSE-bright and BSE-dark domains of the calcite were analyzed. The results show that the former has CaO (52.75–55.05 wt%) and REE (240–370 ppm) higher but Na (44.1–64.4 ppm), Mg (910–2346 ppm), Mn (1688–5018 ppm), and Fe (3350–14 204 ppm) lower than the latter (Figs. 6a and 6b; Online Material[1] Tables OM3 and OM4). In total, both domains have comparable Sr contents, but in the case of an individual calcite grain, the BSE-bright domain tends to have relatively high Sr. Both domains exhibit similarly LREE-enriched, right-dipping chondrite-normalized REE patterns, but the BSE-dark domains have relatively low-LREE contents and $(La/Yb)_N$ ratios (Fig. 6c), which is particularly remarkable for individual calcite. In contrast, both domains have similar HREE concentrations and exhibit similarly positive Eu anomalies with δEu varying from 1.06 to 1.34 (Online Material[1] Fig. OM2).

Phengite and chlorite chemistry

Both phengite and chlorite from the late hydrothermal stage were analyzed for major elemental compositions. The phengite grains are F-rich (0.12–1.18 wt%) (Online Material[1] Table OM5), and have limit variations of K_2O (10.34–10.94 wt%), SiO_2 (48.77–51.99 wt%), Al_2O_3 (26.69–31.84 wt%), MgO (1.42–3.33 wt%), and FeO (3.15–4.18 wt%). The chlorite grains have much lower F and Cl (both <0.02 wt%) (Online Material[1] Table OM5), and exhibit relatively large variations in SiO_2 (22.77–25.03 wt%), Al_2O_3 (18.95–23.39 wt%), MgO (5.07–11.46 wt%), and FeO (28.76–38.52 wt%).

IN-SITU SR AND ND ISOTOPES OF MINERALS

Detailed methods for in situ Sr-Nd isotopic analyses of apatite, monazite, and bastnäsite are provided in the Online Material[1] Methods, and the results are given in Online Material[1] Table OM6–OM9.
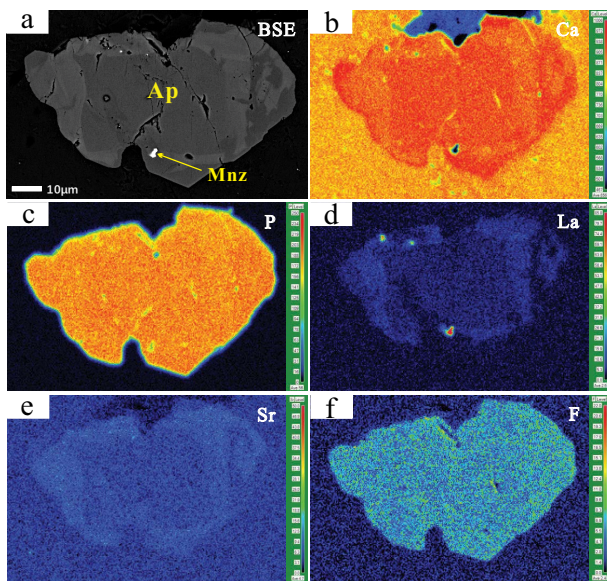

FIGURE 7. Elemental mapping of an apatite grain from the carbonatites, showing the distribution patterns of Ca, P, La, Sr, and F in the grain. (Color online.)

Sr-Nd isotopes of apatite

All the domains have extremely low $^{87}Rb/^{87}Sr$, consistent with their low Rb but high Sr concentrations (Online Material[1] Table OM2). The $^{87}Sr/^{86}Sr$ ratios of the BSE-bright domains in apatite range from 0.70360 to 0.70389, which are broadly identical to those of the BSE-dark domains (I and II) (Fig. 8; Online Material[1] Table OM6). In addition, the BSE-bright domains have $^{147}Sm/^{144}Nd$ and $^{143}Nd/^{144}Nd$ ratios ranging from 0.09064 to 0.10809 and 0.51227 to 0.51251, respectively, similar to those of the BSE-dark-I domains, but slightly lower than those of the BSE-dark-II domains with $^{147}Sm/^{144}Nd$ and $^{143}Nd/^{144}Nd$ varying from 0.10600 to 0.25732 and 0.51243 to 0.51263, respectively (Online Material[1] Table OM7). On the basis of the obtained ages of ~220 Ma for the REE minerals (Xu et al. 2014; Ying et al. 2017; Zhang et al. 2019a), we calculated the $\varepsilon_{Nd}(t)$ values by using the formula of $[(^{143}Nd/^{144}Nd)_{sample}(t)/(^{143}Nd/^{144}Nd)_{CHUR}(t)-1] \times 10\,000$, for different domains in the apatite grains. The results show that the $\varepsilon_{Nd}(t)$ values of the BSE-bright domains range from –4.58 to 0.03, broadly comparable to those of the BSE-dark-I (–3.66 to 0.19) and BSE-dark-II (–4.63 to 0.36) domains (Fig. 9a).

Nd isotopes of monazite and bastnäsite

Three types of monazite grains, including those associated with apatite, those occurring as a disseminated crystal, and those in veinlets, were selected for in situ Nd isotopic analyses. The monazite grains associated with apatite, including those inside and outside the apatite hosts, have similar $^{147}Sm/^{144}Nd$ and $^{143}Nd/^{144}Nd$ ratios ranging from 0.05674 to 0.08416 and 0.51240 to 0.51247, respectively. These ratios are broadly identical to those of the monazite grains in the disseminated crystals and veinlets (Online Material[1] Table OM8). Using the age of ~220 Ma, the calculated $\varepsilon_{Nd}(t)$ values for the monazite associated with apatite have a limited variation (–1.18 to 0.30) that are indistinguishable from those of the disseminated monazite (–2.03 to –0.27) and in those found in the veinlets (–1.23 to –0.06) (Fig. 9b).

Bastnäsite grains, disseminated and in veinlets, have similarly limited variations of $^{147}Sm/^{144}Nd$ (0.06639–0.09764) and
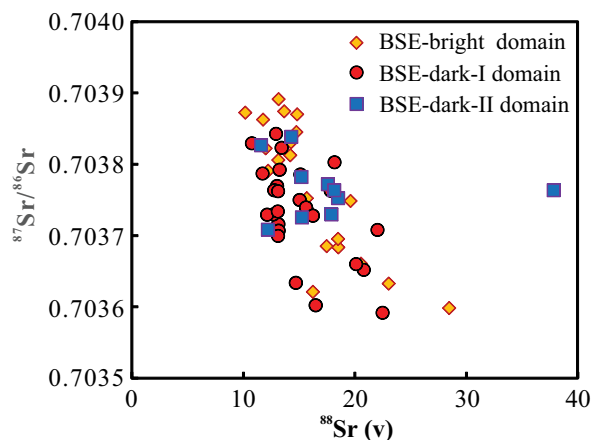

FIGURE 8. Plots of in situ $^{87}Sr/^{86}Sr$ vs. ^{88}Sr (v) values from the BSE-bright and BSE-dark I and -II areas in the apatite. Note that ^{88}Sr (v) represents the Sr signal intensities during analyses. (Color online.)
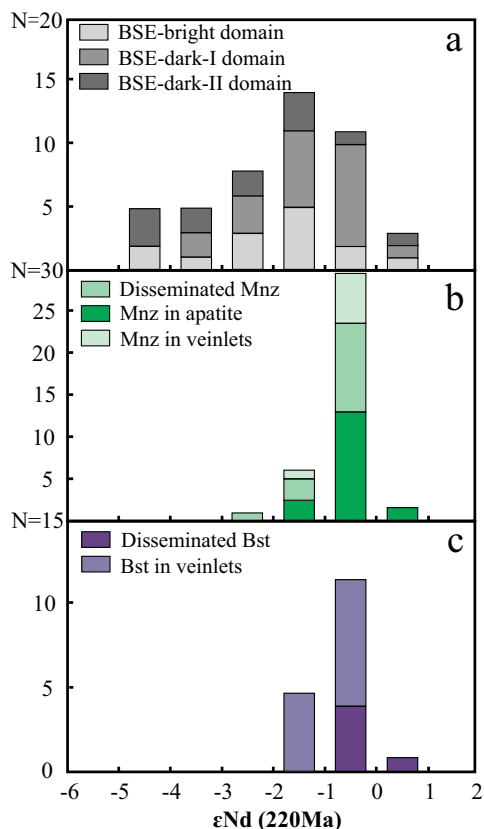
Figure 9. Histograms showing ε_{Nd} ($t = 220$ Ma) values for different areas in the apatite (**a**), various monazites (**b**), and bastnäsite (**c**). Note: $\varepsilon_{Nd}(t)$ values are calculated based on the age of 220 Ma; $\varepsilon_{Nd}(t) = [(^{143}Nd/^{144}Nd)_S(t)/(^{143}Nd/^{144}Nd)_{CHUR}(t) - 1] \times 10\,000$; where S = sample, $(^{143}Nd/^{144}Nd)_{CHUR} = 0.512638$, $(^{147}Sm/^{144}Nd)_{CHUR} = 0.1967$. (Color online.)

$^{143}Nd/^{144}Nd$ (0.51238–0.51249), corresponding to the calculated $\varepsilon_{Nd}(t)$ values ($t = 220$ Ma) ranging from –0.52 to 0.50 and –1.70 to –0.23, respectively (Online Material[1] Table OM9; Fig. 9c). Such $\varepsilon_{Nd}(t)$ values are also comparable to those of the monazite from the diverse types mentioned above.

Fluid inclusion microthermometry and Raman spectroscope

Fluid inclusions in the apatite BSE-dark domains were investigated to understand the nature of the late hydrothermal fluids (Fig. 10a). Detailed methods for microthermometric and Raman spectroscopic analyses of the fluid inclusions are provided in Online Material[1] Methods. The fluid inclusions are elliptical or irregular in shape, with sizes ranging from 2 to 8 μm (Figs. 10b and 10c). They are commonly two-phase, liquid-rich inclusions with the vapor bubbles occupying 8–37 vol% (Figs. 10–10c). Raman spectroscopic analyses show that there are two peaks around 1284 and 1387 cm^{-1}, indicating that CO_2 is the major vapor phase (Fig. 10d). Most of the fluid inclusions were observed to contain a clathrate, which decomposed at 5.1 to 9.3 °C, corresponding to salinities of 1.42 to 8.82 wt% NaCl equiv. (Fig. 10f) and homogenization temperatures of 226 to 340 °C (Fig. 10e; Online Material[1] Table OM10).

Discussion

Fluid-aided remobilization of early cumulated light REEs in the Miaoya complex

Both apatite and calcite are the dominant primary magmatic, REE-bearing minerals in the early carbonatites and/or syenites. Our textural observations show that the two minerals exhibit similar internal textures that are characterized by the presence of several domains with distinguishable appearances (Figs. 3a–3e). Similar textures, particularly the monazite-bearing apatite, have been replicated in experiments involving mineral-fluid interaction (Harlov et al. 2002b, 2005; Harlov and Förster 2003). These textures have also commonly been observed in some iron oxide-apatite and iron oxide copper-gold deposits (Harlov et al. 2002a; Chen and Zhou 2015; Li and Zhou 2015; Zeng et al. 2016). These textures have been demonstrated to form via a fluid-aided, coupled dissolution-reprecipitation process during which the REEs have been hydrothermally remobilized to form REE minerals such as monazite (Harlov et al. 2002a; Chen and Zhou 2015; Li and Zhou 2015). In the case of Miaoya, the BSE-dark domains (including both I and II) in the apatite and calcite host abundant microporosity, fluid inclusions, and mineral inclusions, compared to the BSE-bright domains that are homogeneous and free of pores and mineral inclusions (Figs. 3b–3e). These features indicate that the BSE dark domains formed from the bright domains (original apatite) through fluid infiltration and chemical alteration, as observed in the experiments (e.g., Harlov et al. 2002a). It is also notable that some of the apatite grains contain both BSE-dark-I and -II domains (Figs. 3c–3e), indicating variable degrees of metasomatic alteration possibly related to consecutive infiltration of fluids.

Both the BSE-dark-I and -II domains in the apatite and the calcite grains have REE concentrations that are lower than the BSE-bright domains, indicating that the REEs have been extensively mobilized and leached from the original apatite during metasomatic alteration. In particular, the BSE-dark domains are depleted in light REE, indicating that the light REEs were more mobile than the heavy REEs that in many grains are only slightly modified (Fig. 5). In addition to the light REEs, the BSE-dark domains in the apatite are also depleted in Y, Na, and Sr relative to the BSE-bright domains (Fig. 7). It is notable that REE+Y in these domains vary positively with Na and Sr but negatively with Ca (Figs. 4c–4e), indicating that these elements were incorporated in the apatite through the coupled substitution reaction: $Na^+ + (REE + Y)^{3+} = 2Ca^{2+}$ and $Sr^{2+} = Ca^{2+}$ (Fig. 4d; Roeder et al. 1987; Pan and Fleet 2002; Harlov et al. 2002b, 2005; Harlov and Förster 2003). The leached REEs from the apatite and calcite were re-incorporated back into the monazite inclusions and along the apatite grain rim (Fig. 3) (e.g., Harlov et al. 2002a), or were partially transported outward on scales of meters to be re-deposited as the REE minerals present as disseminations or in veinlets.

Remobilized REEs as the major contribution for the REE mineralization in Miaoya

Although monazite or bastnäsite could have formed during the magmatic stage (Castor 2008), our results confirm that the major REE mineralization in Miaoya is hydrothermal in origin. For example, the REE minerals are present as a dissemination or in veinlets where they closely associated with hydrothermal
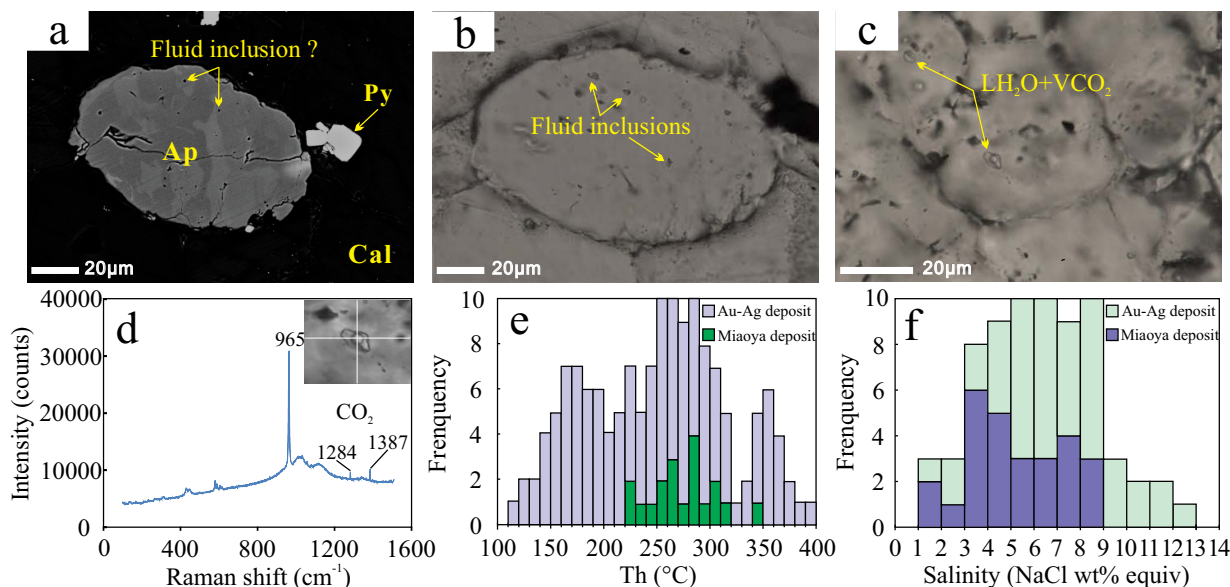
FIGURE 10. Fluid inclusions in the altered apatite. (**a**) BSE image and (**b**) transmit-light image of an altered apatite grain containing abundant fluid inclusions. Also note that small voids are randomly distributed in the grain, possibly representing relics of fluid inclusions. (**c**) Typical fluid inclusions composed of a liquid phase and vapor bubble. (**d**) Laser Raman spectra collected at room temperature for the vapor bubble of the fluid inclusion, showing that the bubbles are rich in CO_2. (**e**) Homogenization temperatures of the fluid inclusions. Also shown are those in quartz from the 220–200 Ma orogenic Au-Ag deposits in the South Qinling unit (data from Feng et al. 1997; Pang et al. 2001; Xu et al. 2012, 2018; Yue et al. 2013). (**f**) Fluid inclusion salinities. Also shown are fluid inclusion salinities from the orogenic Au-Ag deposits (data from Xu et al. 2012; Yue et al. 2013). Abbreviations are the same as those in Figure 2. (Color online.)

minerals (Fig. 3). The monazite grains are characterized by low ThO_2 concentration (typically <0.5 wt%, 0.29 wt% on average; Xu et al. 2010), similar to typical hydrothermal monazite (Schandl and Gorton 2004). Available U-Pb dating of various monazite and bastnäsite have revealed consistent ages of 230 to 210 Ma (Ying et al. 2017; Zhang et al. 2019a). This suggests that REE mobilization and mineralization were coeval and related to a common fluid. However, further evidence is needed to confirm if the major REE mineralization in Miaoya, which occurs either as a dissemination or a veinlet, was also mainly contributed by mobilized REEs, even though most of the carbonatites and syenites in the Miaoya complex have undergone pervasive carbonatization and extensive REE mineralization. To answer this question, we conducted a comparison of Sr-Nd isotopic data from early apatite and REE minerals in multiple stages and various occurrences. Mass balance calculations were also conducted to confirm if the remobilized REEs are sufficient for the REE mineralization in Miaoya.

In situ Sr-Nd isotopic constraints. As the analyzed apatite grains have high Sr (3637–17482 ppm), but extremely low Rb (<3.4 ppm), the measured $^{87}Sr/^{86}Sr$ ratios could be used as initial $^{87}Sr/^{86}Sr$ ratios, without further age calibration. Our new results show that the BSE-dark domains I and II in apatite have $^{87}Sr/^{86}Sr$ ratios and $\varepsilon_{Nd}(t)$ values similar to the primary apatite, i.e., BSE-bright domains (Figs. 8 and 9a), indicating that the causative fluids do not contain enough Sr and Nd to sufficiently modify the initial Sr and Nd isotopic ratios of the primary apatite, or else the fluids have Sr and Nd isotopic compositions similar to the apatite precursors. The latter possibility, however, is unlikely, since the newly obtained $\varepsilon_{Nd}(t)$ values for monazite and bastnäsite in the altered apatite, and as disseminations or veinlets (–2.03 to 0.50)

are similar to those of the BSE-bright or BSE-dark domains of the apatite, which ranges from –4.58 to 0.36 (Fig. 9). These features strongly support the idea that REE mineralization in the Miaoya complex was sourced mainly from early cumulated REEs in the magmatic carbonatites and syenites.

Constraint of mass balance calculation. To quantitatively evaluate the overall mass transfer of REEs during remobilization, we also conducted mass balance calculations for the altered apatite and calcite. Following the procedures of Li and Zhou (2017), the calculations were made by assuming that Tm in apatite and Lu in calcite are hydrothermally immobile. At the very beginning, the concentrations of Tm or Lu in the altered domains of the apatite or calcite were normalized to those of the primary ones. On this basis, other elements could also be normalized accordingly, and an enrichment factor for a certain element could be calculated following the formula: $Xm = C_b/(\rho \cdot C_a)$ (Li and Zhou 2017), in which Xm represents the enrichment factor of a certain element, while C_a and C_b are the concentrations of certain elements in the primary and altered domains, respectively. The ρ values are the relative ratios of concentrations of immobile elements (i.e., Tm and Lu) in the altered and primary domains and were calculated to be 1.1 and 0.99 for Tm in apatite and Lu in calcite, respectively. The calculated enrichment factors are provided in Online Material[1] Table OM11 and illustrated in Figure 11. In Figure 11, the solid line for the enrichment factor as 1 defines no gain or loss. Departure from the line defines gain (above the line) or loss (below the line) for a certain element. The calculated results for apatite show that components lost include light REEs (La, Ce, Pr, Nd; 89.8% lost), Na, Sr, Ba, Ga, and Ge, whereas Mg, Al, Si, Zr, Nb, Th, U, Fe, and Mn were variably enriched (Fig. 11a). On the other hand,

components lost in calcite include LREEs (La, Ce, Pr, Nd; 28.3% lost), P, Si, U, Ga, and Ge, whereas Na, K, Nb, Th, Sc, and V are variably enriched (Fig. 11b).

On the basis of the calculated proportions of the LREE losses, we are able to estimate the total amounts of remobilized LREEs from the primary apatite and calcite in the Miaoya complex to confirm if it matches the reported REE reserve in Miaoya. Detailed steps for the calculation are provided in Table 1. First, we know that the carbonatite stocks, which are mostly altered, cover a total area of about 0.49 km^2, whereas the altered syenites cover a total area of about 5.85 km^2. Both rock types extend to a depth of ~640 m below the current surface (Liu et al. 1984). As such, the total volume of the carbonatites and the syenites are calculated to be 3.15×10^8 m^3 and 3.76×10^9 m^3, respectively (Table 1). Second, the total volumes of apatite and calcite in the complex can be estimated on the basis of their contents in the carbonatites and syenites (Table 1). On this basis, using a density (~3.19 ton/m^3) and the average LREE contents (13 660 ppm) for the primary apatite, along with the estimated proportions of LREE losses (89.8%), the remobilized amounts of LREEs from the apatite in the carbonatites and syenites were calculated to be 1.173 and 1.476 Mt, respectively (Table 1). On the other hand, using the density (~2.71 ton/m^3) and average LREE contents (155 ppm) of calcite and the estimated proportions of LREE losses (28.3%), the remobilized amounts of LREEs from calcite in the carbonatites and syenites were calculated to be 0.032 and 0.054 Mt, respectively (Table 1). As such, the total amount of

remobilized LREEs can be calculated to be 2.735 Mt (Table 1). Such a value is much higher than the reported REE$_2$O$_3$ reserve of 1.21 Mt, which is only for those areas >1.2 wt% REE$_2$O$_3$ (Fig. 1d) (Qian and Li 1996). However, if those ores with grades ranging from 0.3 to 1.2 wt% REE$_2$O$_3$ are incorporated (Fig. 1d), the

TABLE 1. Steps of the calculation related the Total mobilized REEs from carbonatites and syenites

	Carbonatites	Syenites
Covering Area (m^2)	4.9×10^5	5.85×10^6
Maximum depth (m)	640	
Maximum volume (m^3)	3.15×10^8	3.76×10^9
Average proportion of apatite	9.5%	1%
Average proportion of calcite	85%	12%
Maximum volume of apatite (m^3)	2.99×10^7	3.76×10^7
Maximum volume of calcite (m^3)	2.68×10^8	4.51×10^8
Remobilized amounts of LREE from apatite (Mt)	1.173	1.476
Remobilized amounts of LREE from calcite (Mt)	0.032	0.054
Remobilized amounts of LREE (Mt)	1.205	1.53
Total amount of remobilized LREE (Mt)	2.735	

Notes: The densities of fluorapatite and calcite are 3.19 ton/m^3 and 2.71 ton/m^3, respectively. Average LREE contents of fluorapatite and calcite are 13 660 and 155 ppm, respectively. We have calculated that about 89.8 and 28.3% of LREEs (La, Ce, Pr, Nd) lost from the primary fluorapatite and calcite, respectively. First, we need to calculate the maximum volume of carbonatites and syenites. Second, maximum volume of apatite and calcite can be calculated based on the average proportion of apatite and calcite, and the maximum volume of carbonatites and syenites. Third, remobilized amounts of LREEs from apatite and calcite can be calculated based on the densities, average LREE contents, estimated proportion of LREE losses and the maximum volume of apatite and calcite. Finally, the sum of the LREE remobilized from apatite and calcite in carbonatites and syenites represents total amount of remobilized LREEs.
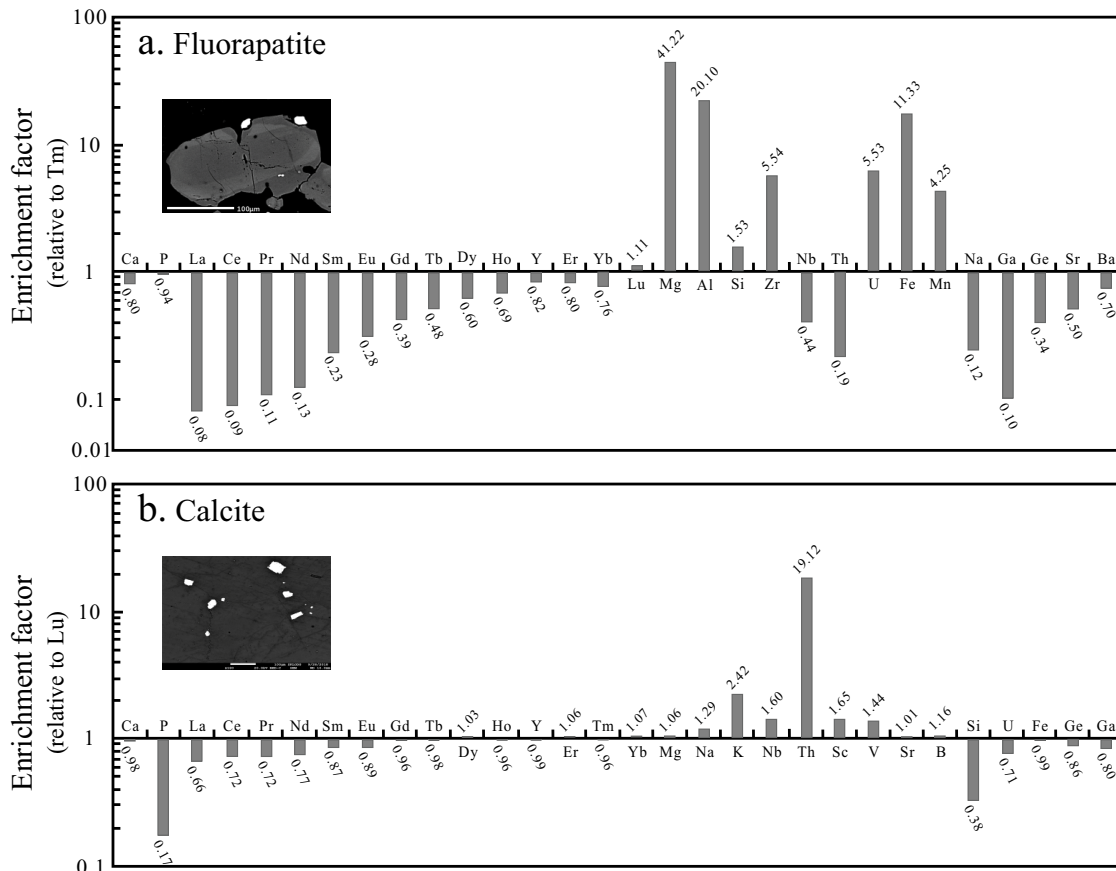

FIGURE 11. Calculated enrichment factors relative to Tm and Lu for various elements during alteration of apatite (**a**) and calcite (**b**).

total reserve, i.e., $REE_2O_3 > 0.3$ wt%, would be much larger and could broadly match the estimated value of the mobilized LREEs (e.g., Fig. 1d). Therefore, our mass balance calculation confirms that early cumulated LREEs, which were mostly in the magmatic apatite and calcite from the complex, were sufficient for the REE mineralization related to late hydrothermal reworking.

Nature and potential sources of the causative fluids

Results from the fluid inclusion study show that the causative fluids responsible for REE remobilization and mineralization are CO_2-rich, with medium temperatures (226–340 °C), and low salinities (1.42–8.82 wt‰) (Fig. 10). The local presence of fluorite and F-rich phengite in the mineralized veinlets imply that the fluids were also rich in F (Online Material[1] Table OM5). All these ligands were well confirmed to be important mediums aiding the mobility of REEs, particularly light REEs (Harlov et al. 2005; Williams-Jones et al. 2012; Williams-Jones and Migdisov 2014; Li et al. 2015; Perry and Gysi 2018). It is thus concluded that such low-salinity, CO_2-, F-, and Cl-rich fluids, presumably unsaturated with REEs, should be responsible for REE mobilization and subsequent mineralization in the Miaoya complex.

The potential sources of the causative fluids have not been addressed previously but can be speculated about due to coeval, 230–210 Ma hydrothermal/mineralization events in the same region. Available studies have revealed that numerous orogenic, 220 to 200 Ma Au-Ag deposits, e.g., Yindonggou, Xujiapo, Shejiayuan, Putang, and Xunyang deposits, are distributed along the South Qinling unit (Chen and Santosh 2014). The ore-forming fluids for these deposits were constrained to be CO_2-rich, with low to medium temperatures and salinities (Feng et al. 1997; Cai et al. 1999; Pang et al. 2001; Xu et al. 2012, 2018; Yue et al. 2013), which are broadly similar to the causative fluids documented in Miaoya (Fig. 10). Moreover, a summary of previous C-O isotopic results from the altered rocks/ores in the Miaoya
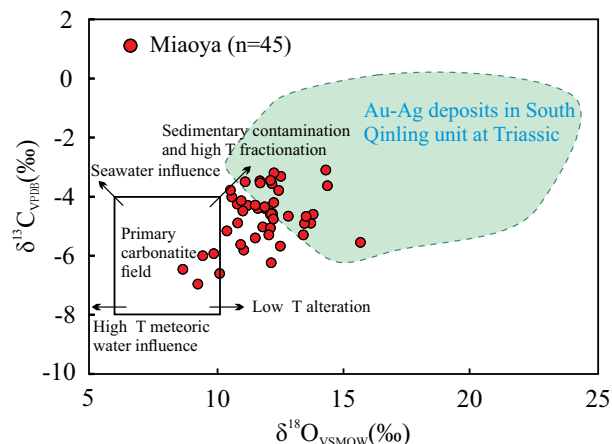

Figure 12. Summary of previous C-O isotopic compositions of carbonate grains from the Miaoya complex (Xu et al. 2014; Cimen et al. 2018; Zhang et al. 2019b; Su et al. 2019). The data for the orogenic Au-Ag deposits in South Qinling unit are cited from Pang et al. (2001), Zhang et al. (2010), and Yue and Deng (2019), whereas the field of primary, mantle-derived carbonates is cited from Taylor et al. (1967). Arrows indicate schematically the major processes responsible for changes in C-O isotopic compositions (Demény et al. 1998). (Color online.)
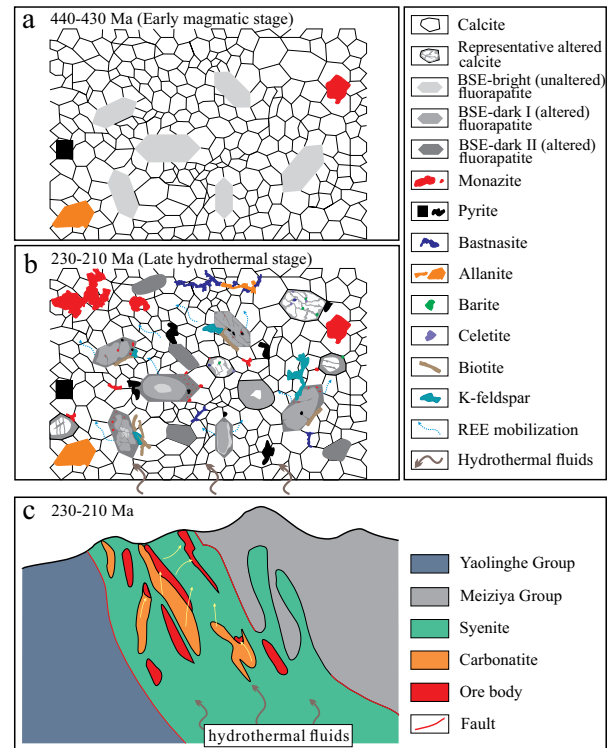

Figure 13. Cartoons illustrating the formation process of the REE mineralization in the Miaoya deposit. (**a**) The carbonatites and syenites in the Miaoya complex formed initially at ca. 440–430 Ma, during which magmatic calcite, apatite, and minor allanite and monazite formed. (**b**) Significant remobilization of early cumulated REEs in apatite and calcite were triggered by the infiltration of external fluids at ca. 220 Ma, responsible for the formation of abundant monazite and bastnäsite. (**c**) At the hydrothermal stage, the early cumulated REEs were remobilized and transported on scales of meters or even possibly tens of meters to be re-deposited as monazite and/or bastnäsite. Further details are available in the text. (Color online.)

complex shows that these data plots the field in between the primary carbonatites and the Au-Ag deposits (Fig. 12) (Xu et al. 2014; Cimen et al. 2018; Su et al. 2019; Zhang et al. 2019b). Such an isotopic feature strongly indicates that the causative fluids are likely coeval and co-genetic with those of the Au-Ag deposits in the same region.

A genetic model for the REE mineralization in the Miaoya complex

This study confirms that the formation of the Miaoya complex and associated REE mineralization involved two separate stages. Both the syenites and carbonatites formed from partial melting of the upper mantle under a rift setting at ~430 Ma (Xu et al. 2014; Zhu et al. 2016; Su et al. 2019; Zhang et al. 2019a), likely followed by a combined fractionation-immiscibility process (Fig. 13a; Su et al. 2019). It is noteworthy that although both the carbonatites and syenites have elevated REE concentrations, our work reveals that the REE-rich minerals formed in this stage were dominantly apatite with minor monazite and/or bastnäsite (<1 vol%). Subsequent infiltration and overprinting

by external fluids during 230–210 Ma (Ying et al. 2017; Zhang et al. 2019a), possibly co-genetic with the coeval orogenic Au-Ag mineralization in the same belt, pervasively metasomatized the early carbonatites and syenites (Fig. 13b). Triggered by metasomatism, the early cumulated REEs were extensively mobilized and transported on scales of meters or even possibly tens of meters to be re-deposited as monazite and/or bastnäsite in the form of dissemination or veinlets (Fig. 13c).

Implications

Numerous carbonatites and/or alkaline rocks are enriched in light REEs, but only a few contain sufficient amounts of REE minerals, here monazite and bastnäsite, for economic exploitation. In most cases, the REEs in carbonatites are distributed in diverse minerals (e.g., carbonates or apatite) that are generally not exploited. Our study provides strong evidence that secondary hydrothermal upgrading of early cumulated REEs under certain conditions is the key for the REE mineralization, i.e., repreciptation of economic REE minerals, in the Miaoya complex. It could also be an important mechanism for REE mineralization in other carbonatite-related deposits, such as the Bayan Obo. In particular, our findings that the causative fluids for REE mineralization are co-genetically related to the orogenic Au-Ag deposits formed during the final collision between the North China and South China Cratons allow us to further speculate that hydrothermal mobilization of REEs could be more widespread than previously documented, particularly for REE deposits present in convergent belts where faults (facilitating fluid migration) and hydrothermal fluids are generally more extensively developed. This suggests that carbonatites and alkaline rocks (or even other REE-rich rocks) distributed in the convergent belts could be potential targets for REE exploration.

Acknowledgments

Funding

References cited

Broom-Fendley, S., Styles, M.T., Appleton, J.D., Gunn, G., and Wall, F. (2016) Evidence for dissolution-repreciptation of apatite and preferential LREE mobility in carbonatite-derived late-stage hydrothermal processes. American Mineralogist, 101, 596–611.

Cai, J.H., Zhang, Y.M., and Fu, J.M. (1999) Study on fluid inclusion within quartz from the Xujiapo gold-silver deposit, Northwest Hubei. Geology Focus and Mineral Resources of South China, 4, 44–49.

Cangelosi, D., Broom-Fendley, S., Banks, D., Morgan, D., and Yardley, B. (2020) Light rare earth element redistribution during hydrothermal alteration at the Okorusu carbonatite complex, Namibia. Mineralogical Magazine, 84, 49–64.

Castor, S. (2008) The Mountain Pass rare-earth carbonatite and associated untrapotassic rocks, California. Canadian Mineralogist, 46, 779–806.

Chen, Y.J., and Santosh, M. (2014) Triassic tectonics and mineral systems in the Qinling Orogen, central China. Geological Journal, 49, 338–358.

Chen, W.T., and Zhou, M.F. (2015) Mineralogical and geochemical constraints on mobilization and mineralization of rare Earth elements in the Lala Fe-Cu-(Mo, Ree) deposit, SW China. American Journal of Science, 315, 671–711.

Cheng, Z.G., Zhang, Z.C., Aibai, A., Kong, W.L., and Holtz, F. (2018) The role of

magmatic and post-magmatic hydrothermal processes on rare-earth element mineralization: A study of the Bachu carbonatites from the Tarim Large Igneous Province, NW China. Lithos, 314-315, 71–87.

Cimen, O., Kuebler, C., Monaco, B., Simonetti, S.S., Corcoran, L., Chen, W., and Simonetti, A. (2018) Boron, carbon, oxygen and radiogenic isotope investigation of carbonatite from the Miaoya complex, Central China: Evidences for late-stage REE hydrothermal event and mantle source heterogeneity. Lithos, 322, 225–237.

Demény, A., Ahijado, A., Casillas, R., and Vennemann, T.W. (1998) Crustal contamination and fluid/rock interaction in the carbonatites of Fuerteventura (Canary Islands, Spain): A C, O, H isotope study. Lithos, 44, 101–115.

Dong, Y.P., and Santosh, M. (2016) Tectonic architecture and multiple orogeny of the Qinling Orogenic Belt, Central China. Gondwana Research, 29, 1–40.

Dong, Y.P., Zhang, G.W., Neubauer, F., Liu, X.M., Genser, J., and Hauzenberger, C. (2011) Tectonic evolution of the Qinling orogen, China: Review and synthesis. Journal of Asian Earth Sciences, 41, 213–237.

Feng, J.Z., Wang, S.L., Ai, X., and Liu, K.M. (1997) Mineralizing physical-chemical condition and fluid evolution in Maotang and Putang gold deposits, Henan. Gold Geology, 3, 17–22 (in Chinese).

Foster, G.L., and Vance, D. (2006) In situ Nd isotopic analysis of geological materials by laser ablation MC-ICP-MS. Journal of Analytical Atomic Spectrometry, 21(3), 288–296.

Gao, J.F., and Zhou, M.F. (2013) Generation and evolution of siliceous high magnesium basaltic magmas in the formation of the Permian Huangshandong intrusion (Xinjiang, NW China). Lithos, 162, 128–139.

Gysi, A.P., and Williams-Jones, A.E. (2013) Hydrothermal mobilization of pegmatite-hosted REE and Zr at Strange Lake, Canada: A reaction path model. Geochimica et Cosmochimica Acta, 122, 324–352.

Harlov, D.E., and Förster, H.J. (2003) Fluid-induced nucleation of (Y+REE)-phosphate minerals within apatite: nature and experiment. Part II. Fluorapatite. American Mineralogist, 88, 1209–1229.

Harlov, D.E., Andersson, U.B., Förster, H.J., Nyström, J.O., Dulski, P., and Broman, C. (2002a) Apatite-monazite relations in the Kiirunavaara magnetiteapatite ore, northern Sweden. Chemical Geology, 191, 47–72.

Harlov, D.E., Förster, H.J., and Nijland, T.G. (2002b) Fluid-induced nucleation of (Y+REE)-phosphate minerals within apatite: Nature and experiment. Part I. Chlorapatite. American Mineralogist, 87, 245–261.

Harlov, D.E., Wirth, R., and Förster, H. (2005) An experimental study of dissolution repreciptation in fluorapatite: Fluid infiltration and the formation of monazite. Contributions to Mineralogy and Petrology, 150, 268–286.

Hou, Z.Q., Liu, Y., Tian, S.H., Yang, Z.M., and Xie, Y.L. (2015) Formation of carbonatite-related giant rare-earth-element deposits by the recycling of marine sediments. Scientific Reports, 5, 10231.

Isnard, H., Brennetot, R., Caussignac, C., Caussignac, N., and Chartier, F. (2005) Investigations for determination of Gd and Sm isotopic compositions in spent nuclear fuels samples by MC ICP-MS. International Journal of Mass Spectrometry, 246, 66–73.

Li, X.C., and Zhou, M.F. (2015) Multiple stages of hydrothermal REE remobilization recorded in fluorapatite in the Paleoproterozoic Yinachang Fe-Cu-(REE) deposit, Southwest China. Geochimica et Cosmochimica Acta, 166, 53–73.

——— (2017) Hydrothermal alteration of monazite-(Ce) and chevkinite-(Ce) from the Sin Quyen Fe-Cu-LREE-Au deposit, northwestern Vietnam. American Mineralogist, 102, 1525–1541.

Li, X.C., Zhao, X.F., Zhou, M.F., Chen, W.T., and Chu, Z.Y. (2015) Fluid inclusion and isotopic constraints on the origin of the Paleoproterozoic Yinachang Fe-Cu-(REE) deposit, southwest China. Economic Geology, 110, 1339–1369.

Li, X.C., Zhou, M.F., Yang, Y.H., Zhao, X.F., and Gao, J.F. (2018) Disturbance of the Sm-Nd isotopic system by metasomatic alteration: A case study of fluorapatite from the Sin Quyen Cu-LREE-Au deposit, Vietnam. American Mineralogist, 103, 1478–1496.

Ling, M.X., Liu, Y.L., Williams, I.S., Teng, F.Z., Yang, X.Y., Ding, X., Wei, G.J., Xie, L.H., Deng, W.F., and Sun, W.D. (2013) Formation of the world's largest REE deposit through protracted fluxing of carbonatite by subduction-derived fluids. Scientific Reports, 3, 1–8.

Liu, Y., and Hou, Z.Q. (2017) A synthesis of mineralization styles with an integrated genetic model of carbonatite-syenite-hosted REE deposits in the Cenozoic Mianning-Dechang REE metallogenic belt, the eastern Tibetan Plateau, southwestern China. Journal of Asian Earth Sciences, 137, 35–79.

Liu, J.Y., Li, S., Hao, Y.W., Zhu, H.M., and Li, G.P. (1984) A study on the carbonatite type Nb-REE ore deposit of Miaoya, Hubei, China, 143 p. Monograph on Mineral Deposit, Hubei (in Chinese).

Liu, Z.C., Wu, F.Y., Yang, Y.H., Yang, J.H., and Wilde, S.A. (2012) Neodymium isotopic compositions of the standard monazites used in U-Th-Pb geochronology. Chemical Geology, 334, 221–239.

Liu, L., Liao, X.Y., Wang, Y.W., Wang, C., Santosh, M., Yang, M., Zhang, C.L., and Chen, D.L. (2016) Early Paleozoic tectonic evolution of the North Qinling Orogenic Belt in Central China: insights on continental deep subduction and multiphase exhumation. Earth Science Reviews, 159, 58–81.

Mariano, A.N. (1989) Economic geology of rare earth elements. In B.R. Lipin and G.A. McKay, Eds., Geochemistry and Mineralogy of Rare Earth Elements. Reviews in Mineralogy, 21, 309–337.

Mattauer, M., Matte, P., Malavieille, J., Tapponnier, P., Maluski, H., Xu, Z.Q., Lu, Y.L., and Tang, Y.Q. (1985) Tectonics of the Qinling belt: Build-up and evolution of eastern Asia. Nature, 317, 496–500.

Meng, Q.R., and Zhang, G.W. (2000) Geologic framework and tectonic evolution of the Qinling orogen, Central China. Tectonophysics, 323, 183–196.

Pan, Y.M., and Fleet, M.E. (2002) Compositions of the apatite-group minerals: substitution mechanisms and controlling factors. Reviews in Mineralogy and Geochemistry, 48, 13–49.

Pandur, K., Kontak, D.J., and Ansdell, K.M. (2014) Hydrothermal evolution in the Hoidas Lake vein-type REE deposit, Saskatchewan, Canada: Constraints from fluid inclusion microthermometry and evaporate mound analysis. Canadian Mineralogist, 52, 717–744.

Pang, Q.B., Jia, W.G., Han, Z.W., and Chen, S.W. (2001) The mineralization conditions for the Hg-Sb-Au deposits in Xunyang distinct, Shangxi Province. Geology and Resources, 10, 91–101 (in Chinese).

Perry, E.P., and Gysi, A.P. (2018) Rare earth elements in mineral deposits: Speciation in hydrothermal fluids and partitioning in calcite. Geofluids, 2018, 5382480.

Qian, D.D., and Li, J.Q. (1996) The discovering history of Chinese deposits: Hubei volume, 177 p. Geological Publishing House, Beijing (in Chinese).

Ramos, F.C., Wolff, J.A., and Tollstrup, D.L. (2004) Measuring $^{87}Sr/^{86}Sr$ variations in minerals and groundmass from basalts using LA-MC-ICP-MS. Chemical Geology, 211, 135–158.

Ratschbacher, L., Hacker, B.R., Calvert, A., Webb, L.E., Grimmer, J.C., McWilliams, M.O., Ireland, T., Dong, S., and Hu, J. (2003) Tectonics of the Qinling (Central China): Tectonostratigraphy, geochronology, and deformation history. Tectonophysics, 366, 1–53.

Roeder, P.L., MacArthur, D., Ma, X.-P., Palmer, G.R., and Mariano, A.N. (1987) Cathodoluminescence and microprobe study of rare-earth elements in apatite. American Mineralogist, 72, 801–811.

Salvi, S., and Williams-Jones, A.E. (1996) The role of hydrothermal processes in concentrating HFSE in the Strange Lake peralkaline complex, northeastern Canada. Geochimica et Cosmochimica Acta, 60, 1917–1932.

Schandl, E.S., and Gorton, M.P. (2004) A textural and geochemical guide to the identification of hydrothermal monazite: Criteria for selection of samples for dating epigenetic hydrothermal ore deposits. Economic Geology, 99, 1027–1035.

Sheard, E.R., Willams-Jones, A.E., Heiligmann, M., Pederson, C., and Trueman, D.L. (2012) Controls on the concentration of zirconium, niobium, and the rare earth elements in the Thor Lake Rare Metal Deposit, Northwest Territories, Canada. Economic Geology, 107, 81–104.

Smith, M.P., Campbell, L.S., and Kynicky, J. (2015) A review of the genesis of the world class Bayan Obo Fe-REE-Nb deposits, Inner Mongolia, China: Multistage processes and outstanding questions. Ore Geology Reviews, 64, 459–476.

Smith, M.P., Moore, K., Kavecsánszki, D., Finch, A.A., Kynicky, J., and Wall, F. (2016) From mantle to critical zone: A review of large and giant sized deposits of the rare earth elements. Geoscience Frontiers, 7, 315–334.

Song, W.L., Xu, C., Smith, M.P., Chakhmouradian, A.R., Brenna, M., Kynicky, J., Chen, W., Yang, Y.H., Deng, M., and Tang, H.Y. (2018) Genesis of the world's largest rare earth element deposit, Bayan Obo, China: Protracted mineralization evolution over ∼1 b.y. Geology, 46, 323–326.

Su, J.H., Zhao, X.F., Li, X.C., Hu, W., Chen, M., and Xiong, Y.L. (2019) Geological and geochemical characteristics of the Miaoya syenitecarbonatite complex, Central China: Implications for the origin of REE-Nb enriched carbonatite. Ore Geology Reviews, 113, 103101.

Taylor, H.P., Frechen, J., and Degens, E.T. (1967) Oxygen and carbon isotope studies of carbonatites from the Laacher See District, West Germany and the Alno District, Sweden. Geochimica et Cosmochimica Acta, 31, 407–430.

Verplanck, P.L., Mariano, A.N., and Mariano, A.J. (2016) Rare earth element ore geology of carbonatites. Reviews in Economic Geology, 18, 5–32.

Williams-Jones, A.E., and Migdisov, A.A. (2014) Rare earth element transport and deposition by hydrothermal fluids. Acta Geologica Sinica (English edition), 88, 472–474.

Williams-Jones, A.E., Migdisov, A.A., and Samson, I.M. (2012) Hydrothermal mobilization of the rare earth elements—a tale of "Ceria" and "Yttria". Elements, 8, 355–360.

Woolley, A.R., and Kjarsgaard, B.A. (2008) Paragenetic types of carbonatite as indicated by the diversity and relative abundances of associated silicate rocks: Evidence from a global database. Canadian Mineralogist, 46, 741–752.

Wu, Y.B., and Zheng, Y.F. (2013) Tectonic evolution of a composite collision orogen: An overview on the Qinling-Tongbai-Hong'an-Dabie-Sulu orogenic belt in Central China. Gondwana Research, 23, 1402–1428.

Xiao, B., Li, Q.G., He, S.Y., Chen, X., Liu, S.W., Wang, Z.Q., Xu, X.Y., and Chen, J.L. (2017) Contrasting geochemical signatures between Upper Triassic Mo-hosting and barren granitoids in the central segment of the South Qinling orogenic belt, central China: Implications for Mo exploration. Ore Geology Reviews, 81, 518–534.

Xie, Y.L., Hou, Z.Q., Yin, S.P., Dominy, S.C., Xu, J.H., Tian, S.H., and Xu, W.Y. (2009) Continuous carbonatitic melt-fluid evolution of a REE mineralization system: Evidence from inclusions in the Maoniuping REE deposit, Western Sichuan, China. Ore Geology Reviews, 36, 90–105.

Xu, C., Campbell, I.H., Allen, C.M., Chen, Y., Huang, Z., Qi, L., Zhang, G., and Yan, Z. (2008) U-Pb zircon age, geochemical and isotopic characteristics of carbonatite and syenite complexes from the Shaxiongdong, China. Lithos, 105, 118–128.

Xu, C., Kynicky, J., Chakhmouradian, A.N., Campbell, I.H., and Allen, C.M. (2010) Trace-element modeling of the magmatic evolution of rare-earth-rich carbonatite from the Miaoya deposit, central China. Lithos, 118, 145–155.

Xu, T.L., Ma, C.P., Lv, X.Z., and Liu, X.Y. (2012) Geological characteristics and prospecting direction of Shejiayuan silver gold deposits in Yunxi Country, Hubei Province. Resources Environment and Engineering, 26, 104–110.

Xu, C., Chakhmouradian, A.R., Taylor, R.N., Kynicky, J., Li, W.B., Song, W.L., and Fletcher, I.R. (2014) Origin of carbonatites in the south Qinling orogen: Implications for crustal recycling and timing of collision between the south and North China blocks. Geochimica et Cosmochimica Acta, 143, 189–206.

Xu, F., Li, W.B., Song, G.S., Wang, M.Z., Kang, Q.Q., Cao, Y., and Zhu, W.P. (2018) Ore-controlling factors and metallogenic model of gold deposit in Shiquan-Xunyang area, Shanxi. Mineral Exploration, 9, 70–78 (in Chinese).

Yang, Y.H., Wu, F.Y., Chu, Z.Y., Xie, L.W., and Yang, J.H. (2013) High-precision simultaneous determination of $^{147}Sm/^{144}Nd$ and $^{143}Nd/^{144}Nd$ ratios in Sm-Nd mixtures using multi-collector inductively coupled plasma-mass spectrometry and its comparison to isotope dilution analysis. Spectrochimica Acta Part B: Atomic Spectroscopy, 79/80, 82–87.

Yang, Y.H., Wu, F.Y., Yang, J.H., Chew, D.M., Xie, L.W., Chu, Z.Y., and Huang, C. (2014) Sr and Nd isotopic compositions of apatite reference materials used in U–Th-Pb geochronology. Chemical Geology, 385, 35–55.

Yang, X.Y., Lai, X.D., Pirajno, F., Liu, Y.L., Ling, M.X., and Sun, W.D. (2017) Genesis of the Bayan Obo Fe-REE-Nb formation in Inner Mongolia, North China Craton: A perspective review. Precambrian Research, 288, 39–71.

Yang, K.F., Fan, H.R., Pirajno, F., and Li, X.C. (2019a) The Banyan Obo (China) giant REE accumulation conundrum elucidated by intense magmatic differentiation of carbonatite. Geology, 47, 1198–1202.

Yang, Y.H., Wu, F.Y., Li, Q.L., Rojas-Agramonte, Y., Yang, J.H., Ma, Q., Xie, L.W., Huang, C., Fan, H.R., Zhao, Z.F., and others. (2019b) In situ U-Th-Pb dating and Sr-Nd isotope analysis of bastnäsite by LA-(MC)-ICP-MS. Geostandards and Geoanalytical Research, 43, 543–565.

Ying, Y.C., Chen, W., Lu, J., Jiang, S.Y., and Yang, Y.H. (2017) In situ U-Th-Pb ages of the Miaoya carbonatite complex in the South Qinling orogenic belt, Central China. Lithos, 290, 159–171.

Ying, Y.C., Chen, W., Simonetti, A., Jiang, S.Y., and Zhao, K.D. (2020) Significance of hydrothermal reworking for REE mineralization associated with carbonatite: Constraints from in situ trace element and C-Sr isotope study of calcite and apatite from the Miaoya carbonatite complex (China). Geochimica et Cosmochimica Acta, 280, 340–359.

Yuan, H.L., Gao, S., Dai, M.N., Zong, C.L., Gunther, D., Fontaine, G.H., Liu, X.M., Diwu, C. (2008) Simultaneous determinations of U-Pb age, Hf isotopes and trace element compositions of zircon by excimer laser-ablation quadrupole and multiple-collector ICP-MS. Chemical Geology, 247, 100–118.

Yue, S.W., and Deng, X.H. (2019) Geological and ore-forming characteristics of Ag-Au and polymetallic deposits in northwestern Hubei, China. Earth Science Frontiers, 26(6), 106–128 (in Chinese).

Yue, S.W., Zhai, Y.Y., Deng, X.H., Yu, J.T., and Yang, L. (2013) Fluid inclusion and H-O isotope geochemistry and ore genesis of the Yindonggou deposit, Zhushan County, Hubei, China. Acta Petrologica Sinica, 29(1), 27–45 (in Chinese).

Zeng, L.P., Zhao, X.F., Li, X.C., Hu, H., and Mcfarlane, C. (2016) In situ elemental and isotopic analysis of fluorapatite from the Taocun magnetite-apatite deposit, Eastern China: Constraints on fluid metasomatism. American Mineralogist, 101, 2468–2483.

Zhang, C.L., Gao, S., Yuan, H.L., Zhang, G.W., Yan, Y.X., Luo, J.L., and Luo, J.H. (2007) Sr-Nd-Pb isotopes of the early Paleozoic mafic-ultramafic dykes and basalts from south Qinling belt and their implications for mantle composition. Science China Earth Science, 50, 1293–1301.

Zhang, Y., Chen, Y.J., Qi, J.P., Leng, C.B., and Zhao, C.H. (2010) Geochemistry of Gongguan-Qingtonggou Hg-Sb deposit in Xunyang, Shaanxi Province. Acta Mineralogica Sinica, 30, 98–106 (in Chinese).

Zhang, W., Chen, W.T., Gao, J.F., Chen, H.K., and Li, J.H. (2019a) Two episodes of REE mineralization in the Qinling Orogenic Belt, Central China: In-situ U-Th-Pb dating of bastnäsite and monazite. Mineralium Deposita, 54, 1365–1280.

Zhang, D.X., Liu, Y., Pan, J.Q., Dai, T.G., and Bayless, R.C. (2019b) Mineralogical and geochemical characteristics of the Miaoya REE Prospect, Qinling Orogenic Belt, China: Insights from Sr-Nd-C-O isotopes and LA-ICP-MS mineral chemistry. Ore Geology Reviews, 110, 102932.

Zhu, J., Wang, L., Peng, S., Peng, L., Wu, C., and Qiu, X. (2016) U-Pb zircon age, geochemical and isotopic characteristics of the Miaoya syenite and carbonatite complex, Central China. Geological Journal, 52, 938–954.

Endnote:

[1]Deposit item AM-21-107779, Online Material. Deposit items are free to all readers and found on the MSA website, via the specific issue's Table of Contents (go to http://www.minsocam.org/MSA/AmMin/TOC/2021/Oct2021_data/Oct2021_data.html).

American Mineralogist: Learn More

Editors: Don Baker and Hongwu Xu

We invite you to submit for publication the results of *original scientific research* in the general fields of mineralogy, crystallography, geochemistry, and petrology. Specific areas of coverage include, but are not restricted to, igneous and metamorphic petrology, experimental mineralogy and petrology, crystal chemistry and crystal-structure determinations, mineral spectroscopy, mineral physics, isotope mineralogy, planetary materials, clay minerals, mineral surfaces, environmental mineralogy, biomineralization, descriptive mineralogy and new mineral descriptions, mineral occurrences and deposits, petrography and petrogenesis, and novel applications of mineralogical apparatus and technique. Am Min also cultivates a number of special collections that are frequently updated.

Submit your paper: https://aminsubmissions.msubmit.net

Information on manuscript preparation:
http://www.minsocam.org/MSA/AmMin/Instructions.html

Am Min website
http://www.minsocam.org/msa/AmMin/AmMineral.html

Quick Facts

• Average submission-to-acceptance time averages ~4 months

• MSA member authors qualify for *free* online color

• Read research articles, reviews, special collections, and more

• Paper Highlights are noted each issue via the MSA talk list, Facebook, and Am Min web page

• Publish with us for high-quality, fast publication, with availability and visiblity worldwide

• Full array of the latest publishing options: e.g., Open access options (both Green and Gold), early publication, reprints, and e-links are all available

• Letters papers submission to acceptance time averages less than 2 months

• Impact Factor 2020: 3.003

Editorial and submission help available at peer_review@minsocam.org